CHAPTER 4

Copper oxide nanoparticle: Multiple functionalities in photothermal therapy and electrochemical energy storage

CHAPTER 4

4.1 Introduction

Nanoparticle of “Copper oxide” which is an important copper based biomineral has gained special attention in scientific community due to its unique physico-chemical characters (e.g. narrow band structure, surface plasmon resonance), and affordable availability of precursor material [165, 292, 293]. However, its effective utilization for the possible treatment of tumor tissues using advanced treatment technique like “photothermal therapy” are limitedly explored. The SPR band of Copper oxide nanoparticle is responsible for enhanced absorption of incident near infrared radiation (NIR). A portion of this incident light is converted it into heat energy according to “Mie theory” [294] and can be utilized as a photothermal agent to destroy cancer cells. The enhanced functionality Copper oxide nanoparticle further extended to the field of electrochemical energy storage systems. Copper oxide being demonstrating excellent redox properties, noticeable semiconducting character, enhanced catalytic and electrical activity, is favorable material of choice for electrode fabrication [295-297]. Now-a-days electrochemical energy storage mainly explored through fabrication of devices such as hybrid-supercapacitor whose efficiency vary in between battery and supercapcitor. It not only exhibits high specific energy as well as power density value but also efficiently stores and delivers “charge” on long cycles of operation.

These all-round applicability in various scientific endeavors already investigated in the past and there is also a current demand for future research in multifunctional Copper oxide nanoparticle. But unfortunately adsorption of toxic and non-polar reagents on the nanoparticle surface during chemical synthesis limit their clinical usage [200, 201] and corrosive substances generated from the spent electrodes also. Green synthesis involving plant extract [118, 198, 298] seems to be advantageous pertaing to its economic viability, facile technique and greater affinity of metal ions towards hydroxyl groups of polyphenols present in the plant extract.[117, 205] Apart from synthesis method, size and morphology control of Copper oxide nanoparticles are highly desirable in nanomedicine research, for effective cellular uptake, bio-distribution and renal clearances.[78] Similarly, morphology and size control of Copper oxide nanoparticle [299, 300] may streamline the process of efficient electrolyte diffusion, reduction of specific resistivity and efficient charge storage in a hybrid supercapacitor.[301]

Hydrothermal method [239] under green synthesis technique is best suited for development of multifunctional Copper oxide nanoparticle by a single step facile approach by mimicking natural biomineralization process. Resulting surface defects [241] in the developed nanoparticle may serve as relaxation centers under light excitation source, for photothermal heat generation [243]. Also these surface defects are known for significantly affecting the electrochemical performance of developed electrode material [301].

Hence the objective of this study to successfully synthesize Copper oxide nanoparticles with controlled morphology and size by suitably selecting the plant material for expediting the process of green synthesis under facile hydrothermal route. Further to evaluate multifaceted applications of developed nanoparticle in cancer treatment and electrochemical energy generation. The photothermal heat generation capability might investigated by irradiating with less expensive 975 nm diode laser. Success of this process might further examined in case of cancer cell lines. Similarly the hybrid supercapacitor electrode potential might explored with the help of three electrode based electrochemical workstation.

4.2 Experimental

4.2.1 Synthesis of CONP from *M.oleifera* Extract

Synthesis of CONP was carried out according to protocol established by our previous research work with slight modification (Fig. 4.1). Prior to synthesis the *M. oleifera* leaf extract was prepared by boiling clean and freshly collected matured leaves from BHU campus in DI water (18 MΩ.cm). The boiling was carried over 2-3h at 90 ºC and prepared yellowish green extract, was filtered using Whatman 1 filter paper. Freshly prepared extract was thoroughly mixed with 10 mM aqueous solution of $CuCl_{2}.2H_{2}O$ (purity > 98.5%, Merck Specialties Pvt. Ltd., India) by magnetically stirring. Subsequently the mixture was transferred into Teflon lined stainless steel autoclave and subjected to hydrothermal reaction for 3h at 120 ºC under continuous stirring.

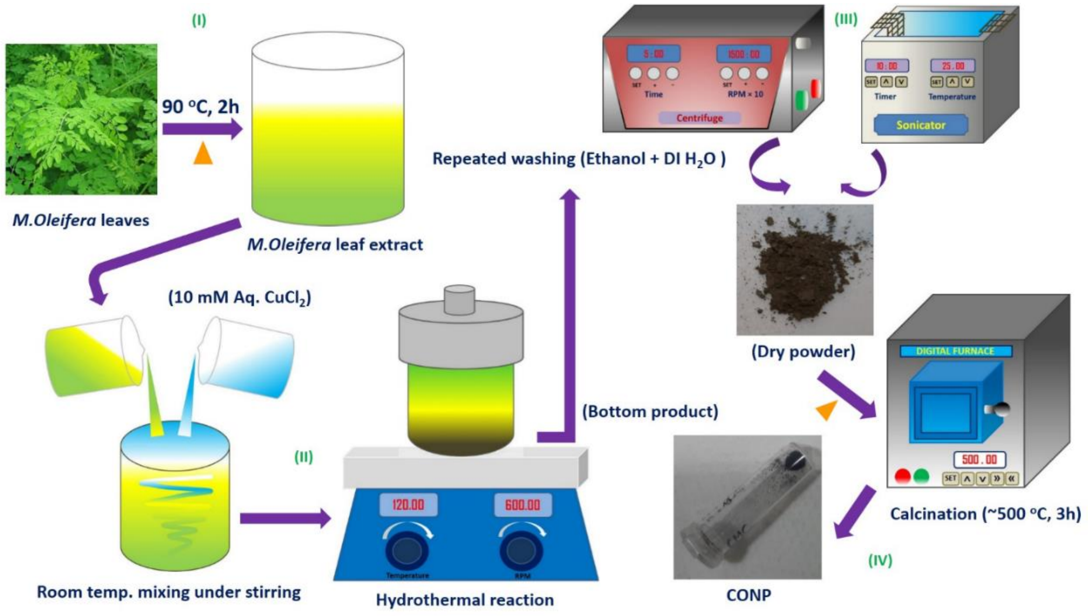

Figure 4.1 Process diagram showing synthesis of CONP from *M.oleifera* leaf extract.

After completion of reaction, the suspension was cooled down and allowed to settle. The bottom dark brown colored precipitate was collected, and washed thoroughly with mixture of ethanol-water under repeated centrifugation and sonication. The dried precipitate was calcined in a digital muffle furnace (NSW works, Varanasi) for about 2h at a temperature of 500 ^{o}C to collect the desired Copper oxide nanoparticle.

4.2.2 Characterizations

Obtained black colored powder after calcination was characterized through X-ray diffraction (XRD) (Rigaku Smart Lab diffractometer) technique (radiation source: CuKα; scanning rate: 3.03 °/min) to ascertain the phase and crystallinity in it. The optical property of synthesized CONP was analyzed with the help of Raman spectroscopy technique (STR-300 spectrometer) with a green laser excitation having excitation wavelength of 532 nm. The morphology and size of prepared nanoparticle was examined via transmission electron microscopy (TEM, FEI TECNAI G^2 20 TWIN). Further FE-SEM analysis was also carried out with the help of electron microscope (FEI NOVA NANOSEM 450, US). The valence states of atoms constituting the basic structure of nanoparticle molecule ascertained through x-ray photoelectron spectroscopy (XPS) (AMICUS, Kratos Analytical). The organic functional groups associated with the nanoparticle was examined by FTIR spectroscopy (Thermo Electron Corporation, USA). The optical absorption nature of prepared nanoparticle was analyzed with the help of "UV-Visible-NIR" Spectrophotometer (Agilent Cary 60, US) in the spectral range of 200-1000 nm. Absorbance was recorded for the aqueous solution of prepared nanoparticle having concentration (~0.06 mg/mL).

4.2.3 Photogenertaed heat study upon NIR exposure

The photo-generated heat was measured by introducing 200µL of aqueous suspension of prepared nanoparticle into a tubular sample holder made up of quartz, attached with a K-type thermocouple and digital temperature indicator (Senstec Thermal controls, Bengaluru India). The two different concentration of nanoparticle suspension (namely

0.01, 0.03 mg/mL) were exposed to 975 nm laser radiation using inexpensive continuous wave diode setup [PSU-III-LED, China]. The laser was operated at 500 mW power with a beam spot size of (≤ 2.5 mm x 5.2 mm), focused on the sample. The rise in temperature was recorded at every 10 sec interval for about 15 minute. Similar experiment was carried out only for DI water as control. For different nanoparticle suspension concentrations, change in temperature (ΔT) was evaluated. The thermal rise experiment was repeated thrice for every sample.

4.2.4 *In Vitro* photothermal study

In Vitro photothermal efficacy of prepared copper based nanoparticle were investigated over B16F10 melanoma cells. The photo-generated heat from prepared nanoparticle upon NIR exposure were experimented for cancer cell death purpose in lab scale. The cytotoxic effect of copper based nanoparticles and additional influence of NIR radiation towards B16F10 melanoma cells were carried out under aseptic conditions.

Prior to thermal ablation study and subsequent viability analysis the requisite chemical reagents were collected. DMEM high glucose, fetal Bovine Serum (FBS), antibiotic penicillin (10.000 U/mL) streptomycin (10 mg/mL), trypsin–EDTA, trypan blue, phosphate buffered saline (PBS), MTT (3-[4,5-dimethyl-thiazol-2-yl]-2,5-diphenyltetrazolium bromide) assay kit were purchased from Himedia. Dimethyl sulfoxide (DMSO) was purchased from Sisco Research Laboratory.

B16F10 melanoma cells were cultured in complete growth medium containing Dulbecco`s Modified Eagles Medium (DMEM) with 10% Fetal Bovine Serum (FBS) and 1% penicillin streptomycin. Briefly saying B16F10 cells in complete growth media were seeded at a density of 5×10^4 cells per well in the 24 well plate and was incubated at 37°C temperature under 5% CO_2 atmosphere in a humidified CO_2 incubator (Galaxy®

170S, Eppendorf Germany) until 60-70% confluency achieved. In the meantime, nanoparticle suspension of known concentration (1 mg/mL) was prepared by addition of growth medium. This nanoparticle suspension was serially diluted by mixing of growth media to obtain different concentration of CONP solution ranging from 0.01-0.1 mg/mL with intermittent interval maintained at 0.05 mg/mL. After attaining the confluence, the culture media in the wells were replaced with the fresh growth medium containg nanoparticles at varying concentrations. Positive control well consisted of cells with complete growth media and negative control comprised of complete growth media devoid of cells. Cells exposed to the nanoparticle were again subjected to subjected to incubation for abut 24h under humidified CO_2 atmosphere in a CO_2 incubator. Both positive as well negative control wells were subjected to thermal radiation by exposing with 975 nm diode laser irradiation for 5 min. During the thermal radiation study two batches of nanoparticle treated B16F10 cells were arranged: one batch was exposed to NIR irradiation for 5 min and the other was kept in dark (no irradiation). The photothermally treated and untreated cells were employed for estimation of IC50 analysis both under irradiation and dark. Furthermore, bright-field images of photothermally treated cells and control sample were acquired using Nikon Ni-U fluorescence microscope.

Successive to thermal treatment process, the wells were washed with PBS solution and then MTT [3-(4, 5-dimethylthiazol-2-yl)-2,5diphenyltetrazolium bromide] containing solution was added. MTT containing solution comprises of 90 % of fresh growth media and 10% of 5mg/mL of MTT in PBS. The well plate was covered with aluminium foil and kept in the CO_2 incubator for 4 h. The complete media with MTT was removed and replaced with dimethyl sulfoxide (DMSO) which dissolves the formazan crystals. Absorbance of the samples was taken at 570 nm in a multimode reader (Synergy H1 hybrid, Biotek, USA). The cytotoxic effect of nanoparticle and combination of NIR radiation + nanoparticle, towards B16F10 cancer cells were interpreted as percent cell viability with respect to the control sample. Statistical analyses were carried out with two way ANOVA technique using GRAPHPAD PRISM software.

4.2.5 Electrochemical Analysis

The electrochemical characterization (e.g. cyclic and square wave voltammetry, galvanostatic charge discharge, EIS) of prepared nanoparticle was performed using a three electrode system electrochemical workstation (VersaSTAT 3 Potentiostat-Galvanostat, AMETEK scientific instruments USA). The three electrode system comprised of Ag/AgCl as reference electrode with platinum and prepared nanoparticle as counter and working electrode respectively. Prior to electrochemical analysis, working electrode was prepared with active surface area (~1.7 mg of deposited nanoparticle/cm^2). Briefly electrode fabrication was accomplished by drop casting of requisite volume of active material suspension (2.5 mg nanoparticle dispersed in 50 μL ethanol) in which ~10 μL Nafion, used as binder. The substrate used was glossy carbon paper (area: 0.5 cm^2) subjected to vacuum drying after active material deposition. To this electrode copper wire was adhered with the help of silver paste to be acted as current collector. Electrical insulation of exposed area of electrode was maintained by applying glue-stick over it. Furthermore 1M KOH was employed as electrolyte entire electrochemical performance analysis.

The electrochemical impedance spectroscopy (EIS) of nanoparticle was examined via, application of 10 mV AC voltage amplitude over a frequency of 100 kHz to 0.1 Hz. The electrochemical active surface area (EASA) was ascertained from the cyclic voltammetry (CV) analysis performed at open circuit potential. The CV curves were obtained in a non-faradic region (-0.2 to -0.1 V) corresponding to the nature of prepared nanomaterial and scan rates were varied from 10 to 80 mV/sec.

4.3 Result & Discussion

4.3.1 Physicochemical Characterization of prepared nanoparticle

The X-Ray diffraction of Copper oxide nanoparticle confirmed its crystalline nature (Fig. 4.2a). Most of the diffraction peaks match with the monoclinic cupric oxide phase (CuO) with lattice parameters of a =4.653 Å, b=3.410 Å, c= 5.108 Å (JCPDS Card No. 98-009-2192). Although, few peaks corresponding to 2θ value of 52.18.and 61.49° indicate presence of small amount of cuprous oxide (Cu_2O) impurity (JCPDS card no. 98-009-6117). Slight shift in cupric oxide diffraction pattern might be due to this impurity phase developed simultaneously. Major diffraction peaks of Copper oxide nanoparticle indicate that, majority of the growth are oriented along (11-1), (111), (20-2) and (002) crystal planes.

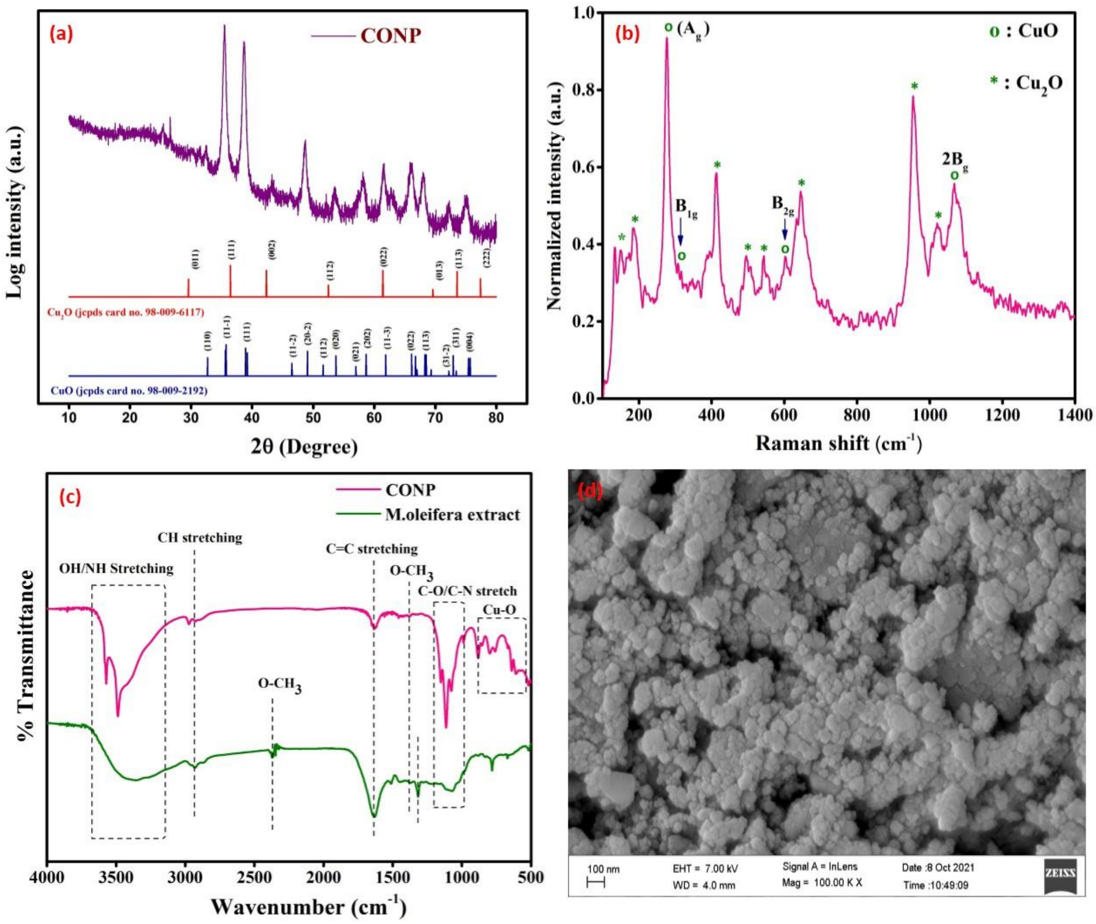

Figure 4.2 (a) HR-XRD and (b) Raman spectra of CONP prepared from *M.oleifera* extract, (c) Corresponding FTIR spectra for surface functionality, (d) FE-SEM image showing morphology.

Taking into account peaks situated at 2θ: 35.56 and 38.67°, the average crystallite size 'D' of Copper oxide nanoparticle (CONP) is calculated using Scherrer formula given by equation 1.

$$D= k*\lambda/\beta*\cos\theta \qquad (1)$$

where D = Crystallite size (nm), k = 0.9 (empirical constant for shape factor), $\lambda = 0.15406$ (wavelength of for CuKα radiation), β = FWHM for the diffraction peak (radian unit), θ = half of the Bragg angle (radian). Using equation-1, CONP crystallites are found to be ~14.3 nm in size.

In terms of degree of crystallinity, cupric oxide (CuO) phase contributed to ~93% while cuprous oxide (Cu_2O) impurity contributed only ~6.3% of overall crystallinity.

The room temperature Raman scattering experiment (Fig. 4.2b) revealed multiple peaks those are closely resembling the existence of both CuO and Cu_2O phases in the synthesized nanoparticle. Out of twelve zone center optical-phonon vibration modes [302] the three Raman active mode observed near ~277, 311 and 604 cm^{-1} correspond to the CuO phase [303]. These pronounced bands denoted as Ag, B_{1g} and B_{2g} modes respectively for CuO crystal [304]. Apart from these three main vibration modes, another multiphonon $2B_g$ band of CuO phase [305] also observed near ~1100 cm^{-1}. The other vibration bands at 148, 188, 411, 493, 540, 645, 1022 cm^{-1} corroborate simultaneous existence of Cu_2O phase [306-308]. It is important to mention here that there is slight variation in position as well as intensity of designated Raman peaks in comparison with the established literatures. There are number of factors modulating the resulting response: morphology, grain size, particle agglomeration, crystal defects etc. [309] Further due to formation of probable defect states by hydrothermal method disappearance of some Raman active modes and appearance of unintended bands is quite obvious. [310]

Organic functional groups associated with CONP, prepared using *M.oleifera* leaf extract ascertained via FTIR spectroscopy. In a comparative manner the functional groups related to *M.oleifera* leaf extract represented along with CONP (Fig. 4.2c). Interestingly majority of organic functionality reflected in CONP indicating possible role of leaf phytochemicals in CONP synthesis. The FTIR spectra revealed the presence of four major IR bands, centered near ~3500 cm^{-1}, ~1620 cm^{-1}, ~1396 cm^{-1} and 1080 cm^{-1} indicating probable presence of $R-NH_2$ (primary amine)/ OH stretching, C=C, $O-CH_3$, C-O stretching vibration respectively. These FTIR peaks indicate the presence of proteins, polyphenolics, organic acids, methoxy group substituted cyclic acids, and pyrolic compounds in CONP resulting from *M.oleifera* extract. The transmittance peak below 1000 cm^{-1} (finger print region) resulting from metal-oxygen interaction (e.g. Cu-O) from inter atomic vibrations [233]. The transmittance bands, ranging in between 3300-3600/1600-1650 cm^{-1} has been reported to be associated with from surface adsorbed water (OH stretching), lattice oxygen from Cu-O bonding reflected below 900 cm^{-1} [137]. These findings support the formation of Copper oxide nanoparticle with the rich organic functionality obtained via green synthesis.

Morphology analysis of CONP was ascertained by FE-SEM analysis (Fig. 4.2d). The SEM images clearly distinguish formation of spherical shaped nanoparticles evenly spaced over entire micrographic plane. But these particles are agglomerated in between them ultimately reducing the contrast.

Besides FE-SEM, transmission electron microscopy (TEM) analysis was also performed to estimate the morphology and size of CONP (figure 4.3). TEM images revealed formation of ~13.4 nm (Fig.4.3a and b) sized CONP with nearly spherical shape. The estimated size of nanoparticles are close to the size reported by X-ray diffraction analysis. Furthermore, the selected area diffraction analysis (SAED) was used to index the crystal planes present in CONP. SAED (Fig. 4.3c) revealed majority of crystal planes correspond to CuO phase along with a small impurity of Cu_2O. High resolution transmission electron microscopy (HRTEM) demonstrates the lattice fringes associated with certain crystalline region of CONP (Fig. 4.3d). The fringe width of ~0.248 nm matches with the (002) crystal plane of cupric oxide (CuO) system. The small size of (~13 nm) CONP is optimum enough for easy cellular uptake s and thus can be further evaluated for their biological applications [78].

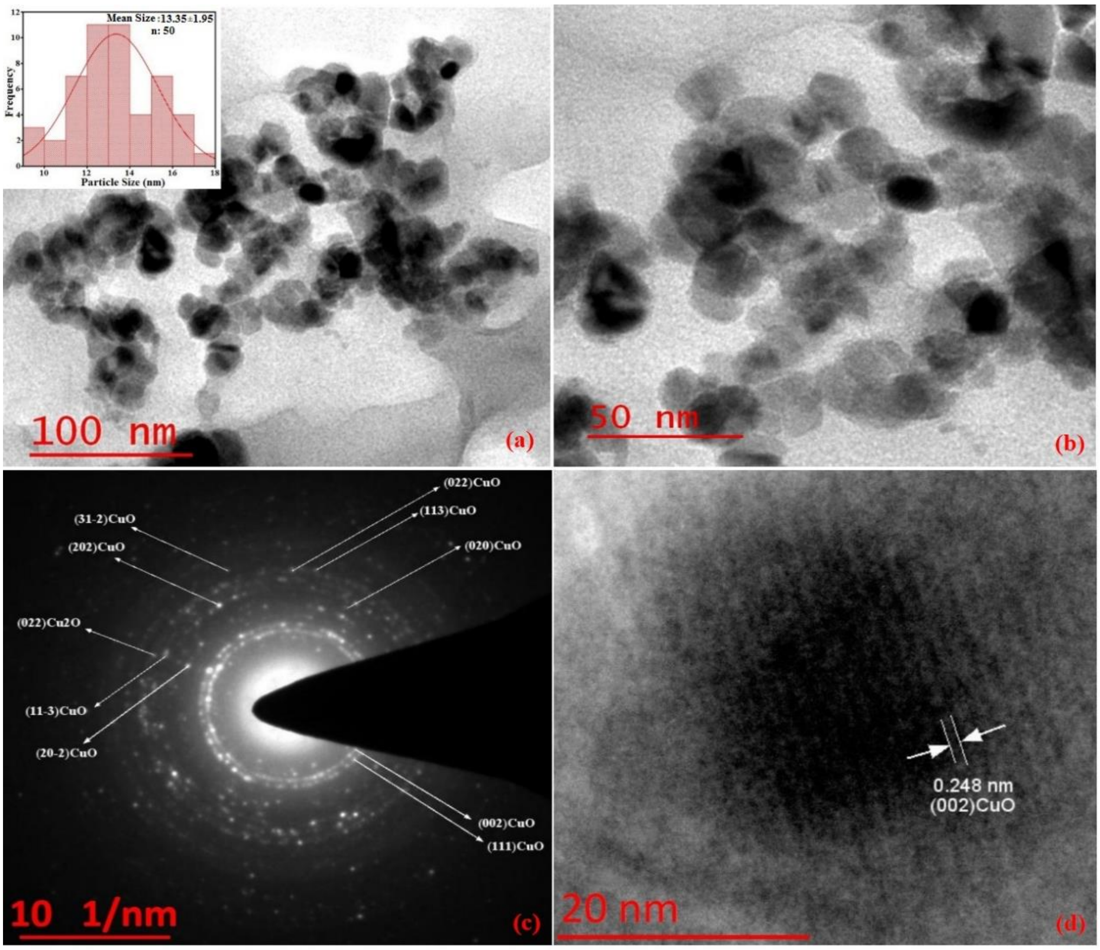

Figure 4.3 (a) & (b) Morphology of CONP. Inset of Fig. 3a showing the size distribution analysis. TEM images of monodispersed FANC. (c) SAED pattern of prepared nanoparticle. (d) HR-TEM analysis revealed the interplaner spacing of Copper oxide nanoparticle.

X-ray Photoelectron spectroscopy (XPS) is a powerful tool to study the transition metal oxide compound like Copper oxide with localized valence d-orbitals. The XPS survey spectra (Fig. 4.4a) of CONP clearly represents profusion of C1s, Cu 2p and O 1s across the entire binding energy range, those are associated with existing Copper oxide system. The C1s peak (Fig. 4.4b) is deconvoluted into four gaussian peaks with 284.8, 285.2, 286.3 and 2888.6 eV binding energies (B.E.), indicating formation of C-C, C-N, C-O and C=O bonds respectively. The XPS spectra of copper element (Fig. 4.4c) resulted two major peaks, positioned at 933.15 and 953.7 eV, correspond to the binding energies (B.E.) of Cu 2p$_{3/2}$ and Cu 2p$_{1/2}$ orbitals respectively. In addition to these two major peaks, there are number of shake up satellite peaks are also observed. The satellite peaks situated at binding energy value of 934.7, 941.4 and 943.8 eV corresponding to $Cu2p_{3/2}$ orbital whereas the satellite peak reflected at higher binding energy i.e. 962.1 eV is the characteristic of $Cu2p_{1/2}$ orbital. These XPS data revealed that copper atom exists in divalent (Cu^{2+}) state pertaining to high binding energy position of $Cu2p_{3/2}$ as well as $Cu2p_{1/2}$ orbitals along with existence of shake up satellite peaks. These satellite peaks help in diagnosis of Cu^{2+} oxidation state because they are related to vacant $3d^9$ shell of divalent copper atom. However due to marginal difference in B.E. (~0.5 eV) between $Cu2p_{3/2}$ orbital of copper atom corresponding to +1 and +2 valence states, the formation of Cu^+ oxidation state cannot be overruled.

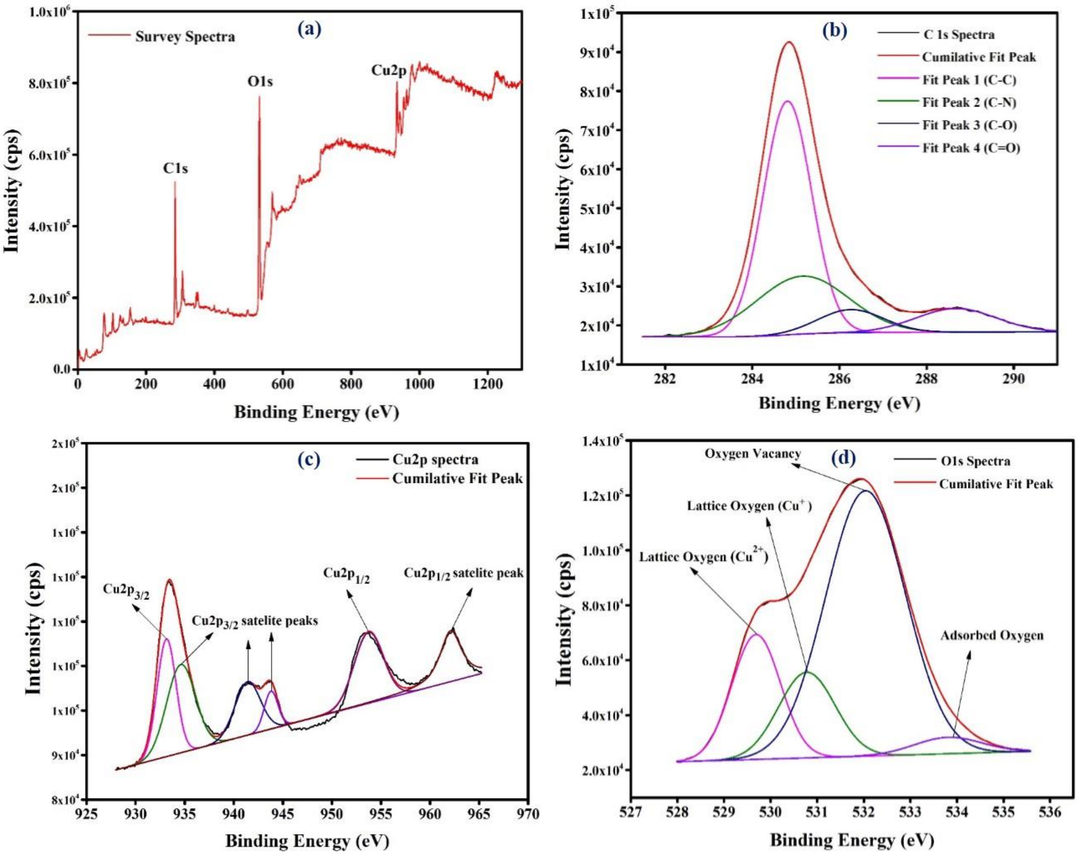

Figure 4.4 XPS spectra of CONP from *M.oleifera* extract (a) Survey spectra (b) C 1S electrons (c) Cu 2p electrons (d) O 1s electrons.

Further, O 1s peak at ~531.93 eV is deconvoluted into four gaussian peaks, representing different types of oxygen ion associated with copper atom during formation of CONP (Fig. 4.4d). The very small peak at ~533. 8 eV indicates the adsorbed oxygen species due to chemisorption or dissociated oxygen ions. Similarly, most intense peak at ~532 eV indicates the oxygen vacancy resulting from surface defects. The major contribution to oxygen spectra is observed largely from lattice oxygen associated withCu_2O (530. 8 eV) or CuO (529.7 eV) species. Overall XPS analyses revealed the formation of cupric oxide (CuO) nanoparticle with simultaneous development of cuprous oxide (Cu_2O) impurity during green synthesis. This observation instigates formulation of possible reaction mechanism taking place during the formation of CONP.

Quantification of both the cuprous and cupric oxide phases by area intensity analysis corresponding to different binding energy values was obtained after de-convolution of copper spectra and details provided in *Appendix* B1. Briefly saying the amount of CuO to Cu_2O phases are distributed in 80 to 20 % ratio.

By taking into account all possible phytochemicals present in in leaf extract, a mechanism has been formulated for the preparation of CONP. nanoparticle (Fig. 4.5) Phytochemicals in *M.oleifera* leaf extracts such as, ascorbic acid, quercetin, and chlorogenic acid under acidic conditions (pH of extract measured to be < 4) undergo oxidation reactions ultimately forming complex with divalent copper cation. The complex formed on subsequent calcination at high-temperature (~500 ^{o}C) resulted CONP enriched with CuO phase [233].

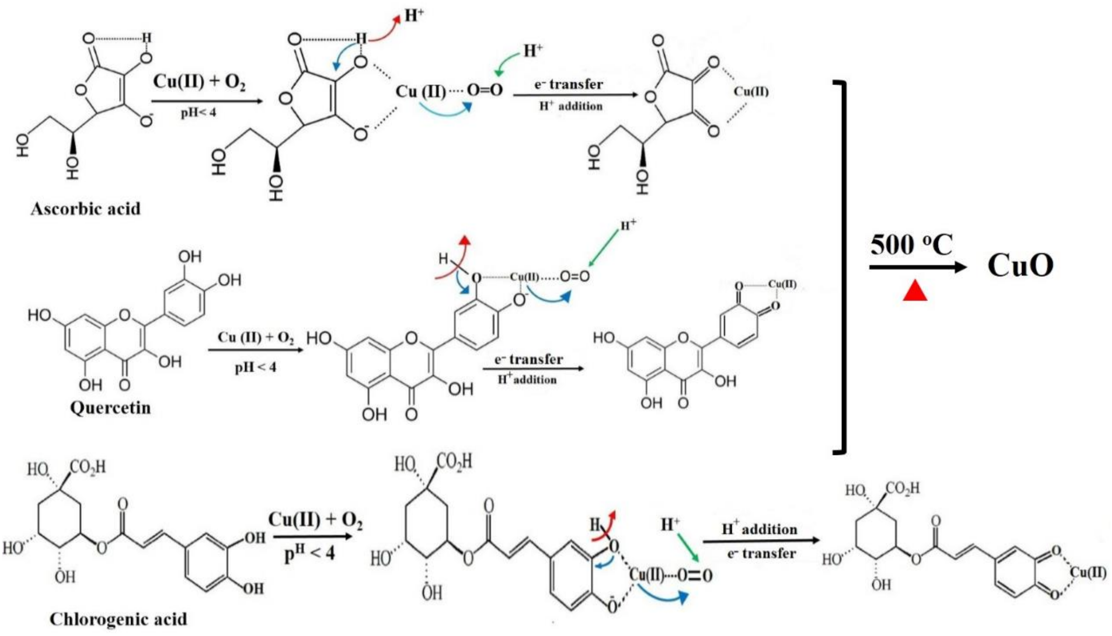

Figure 4.5 Possible reaction mechanism for formation of CuO from *M.oleifera* leaf extract

4.3.2 Optical absorption property

The initial assessment of CONP using TEM, XRD ascertained formation of ~13 nm sized CONP. Previous researches on green synthesized Copper oxide have shown that nanoparticles as big as 13 nm clearly demonstrate presence of SPR band [158, 159, 163] on them, which could play pivotal role in photothermal heat generation. Further the optical absorption property of aqueous Copper oxide nanoparticle is very much important for ascertaining the band positioning and nature of band transition of the prepared semiconductor. It is not only helpful for examining the heat generating capability as earlier describe upon NIR irradiation but also helpful for development devices with energy storage potential. It is observed that CONP absorbs maximum light at 360 nm (Fig 4.6a) due to interband transition of the core electrons associated with CuO nanoparticle [311, 312]. It is important to mention that the absorbance in 300 nm region appears due to cuprous oxide (Cu_2O) impurity formed simultaneously [237].

Further, it is observed that another absorbance maxima occurs at 485 nm due to band edge emission of from CuO [313]. Whereas the broad absorbance band between 300-800 nm can be attributed to the SPR band of CONP (CuO) due to collective oscillation of free lying conduction electrons in the visible light and formation of slightly non-uniform spherical nanoparticles [292, 314-316].Interestingly SPR band is the characteristic of metal oxide structure [100]. It is noticeable that that there is weak optical absorption near-infrared region, which might have resulted due to multiphonon absorption process.

Copper oxide in bulk possess both direct (2-4 eV) as well as indirect band transition (1-1.4 eV) [317]. Upon size reduction, during nanoscale synthesis, dominance of fraction of surface atoms give rise to interesting photophysical properties. Generally a photon impinged on a semiconductor material is absorbed when the incident energy is sufficient enough for transfer of exciton from valence to conduction band and this energy is known as bandgap [318]. Due to size confinement the electronic band structure changes into molecular level structure with non-diminishing energy spacing thus there is overall enhancement in band gap in direct (4.63 eV) as well as and indirect band gap (2.45 eV). This can be seen in Tauc plot (Fig. 4.6a inset), where the band is red shifted due to quantum confinement. Besides the rise in band gap energy can be corroborated with the development of intergap states between valence and conduction band during synthesis of nanoparticle [319]. Further, the dual band gap structure may arose due to the polycrystalline nature of the developed CONP [259]. However linear extrapolation of Tauc plot is fitted well with the direct allowed transition nature of synthesized nanoparticle, again confirming the formation of majority of cupric oxide phases during green synthesis. Further, it is important to note that the indirect band gap present in the CONP is responsible for the generating heat, when exciting radiation with appropriate energy falls on the CONP. This is due to the disparity in crystal momentum vector (k), which prohibits electron-hole recombination, conversing exciting electromagnetic radiation into heat via non-radiative process.

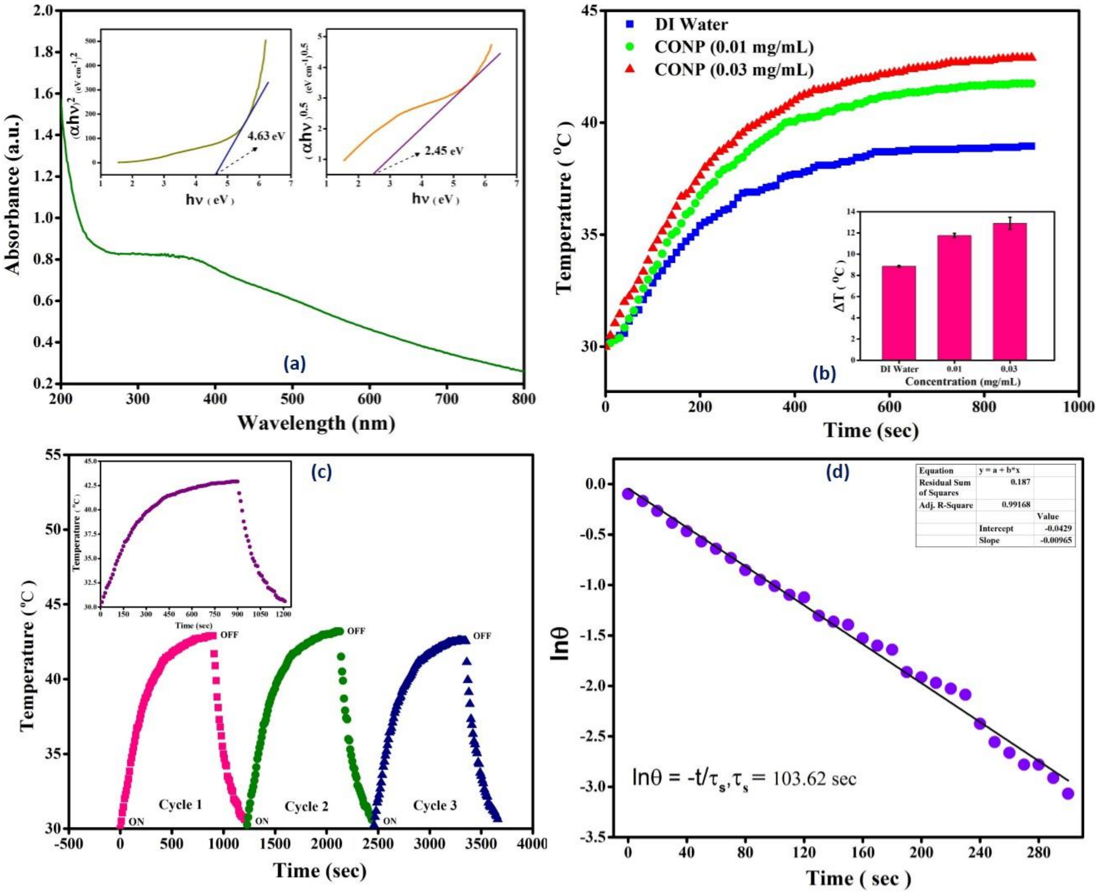

Equation	y = a + b*x	
Residual Sum of Squares	0.187	
Adj. R-Square	0.99168	
		Value
	Intercept	-0.0429
	Slope	-0.00965

Figure 4.6 (a) UV-Visible absorbance spectra of CONP. Inset showing optical band gap values. (b) Temperature rise of aqueous suspension of Copper oxide nanoparticle upon NIR irradiation. Inset showing temperature difference and heat generation stability.

Since our absorption studies shows existence of indirect band gap transition in the developed CONP, thus further evaluation of photothermal heat generation process is taken up.

4.3.3 Photothermal heat generation

Photothermal heat generation was evaluated by irradiating CONP aqueous suspension and plane DI water with (~975 nm) NIR radiation. The rise in temperature with time variation is plotted and represented in Fig 6b. It is observed that the aqueous suspension of CONP generate temperature as high as 43^{o} within 15 min of laser exposure (Fig. 4.6b). The heat generation rate in case of CONP suspension is calculated to be ~1.3^{o}/min, which is high in comparison to DI water having temperature generation rate of ~0.86^{o}/min. The results indicate the satisfactory photothermal heat generation capability of CONP. The temperature rise achieved by the CONP is ~13^{o} greater than the room temperature. Further photothermal heat generation by CONP at different suspension concentration (10-50 ppm) was also evaluated as shown in figure 4.6b. The data represented in figure 4.6c shows excellent thermal stability of CONP at different cycle heating cooling operations. The photothermal heat generation behavior of CONP therefore further needs evaluation of its potential to act like photothermal agent to destroy the cancerous cells. Prior to biological study it is very much important to evaluate the photothermal conversion efficiency (η).

The photothermal conversion efficiency of developed CONP upon 975 nm laser efficiency was calculated according to following equation [320].

$$\eta = \frac{hS\,(T_{max} - T_{amb}) - Q_s}{I(1-10^{-A_{975}})} \tag{2}$$

In equation 2 ‘h’ is the heat transfer coefficient, S stands for the surface area of the tubular sample holder. Similarly, T_{max} and T_{amb} are maximum steady state temperature attained by CONP suspension and ambient temperature respectively. ‘I’ is the incident laser power density with A_{975} denominating the absorbance of CONP suspension (0.03 mg/mL) corresponding to 975 nm laser excitation.

For the given spot size the incident laser power density is calculated to be ~3.5 W/cm^2. 'Q_s' describes amount of heat absorbed, dissipated by solvent and container. By considering pure DI water in tubular quartz container, Q_s independently measured to be ~10 mW.

In order to obtain the value of 'hS', a dimensionless parameter 'θ' is introduced and defined in equation 3 [321].

$$\theta = \frac{T - T_{surround}}{T_{max} - T_{surround}} \tag{3}$$

This dimensionless parameter in equation 3 leads to calculation of time constant (τ_s) which defines the time constant for heat transfer from the system under study. The value of time constant (τ_s) calculated from variation in the temperature of CONP suspension with time (Fig. 4.6d) when the laser excitation is removed [322].

By calculating τ_s, the value of 'hS' obtained from the formula mentioned below [323].

$$hS = \frac{\sum m_i C_{pi}}{\tau_s} \tag{4}$$

where m_i, and C_{pi} stand for mass and heat capacity of individual components (DI water, tubular quartz sample holder) respectively. Additionally mass of DI water and tubular quartz container are measured to be 0.199 and 0.25 gm respectively.

For DI water and Quartz sample holder the value of C_{pi} taken as 4.2 and 0.892 Jg^{-1}K^{-1} respectively.

Therefore by using equation 2. Photothermal conversion efficiency of CONP is calculated to be 22.6 %.

4.3.4 Photothermal ablation of B16F10 cancer cell lines

The CONP capability to kill skin melanoma cell lines (B16F10) by photothermal heat generation using NIR light exposure was investigated, and results are shown in fig. 7 and 8. After 24h incubation with the different concentration of CONP suspension B16F10 cells were subjected to photothermal heating by exposing with 975 nm NIR irradiation. The morphology changes in cancer cell lines after 5 min of thermal effect were also recorded both in presence and without presence of CONP (Fig. 4.7). The cell lines grown without treatment of CONP suspension are addressed as negative and positive control respectively depending on NIR exposure. Fully developed growth of cancer cell lines in media is clearly visible by the representation of elongated morphology (Fig. 4.7a) cited as negative control. When control sample subjected to NIR irradiation (positive control) the cell morphology was remain unchanged by virtue of the fact that cells are transparent to NIR radiation (Fig. 4.7d). Upon incubation with the 0.01 mg/mL of CONP suspension the elongated morphology of cancer cells turned out to be slightly rounded in shape (Fig. 4.7b) indicating cytotoxic effect of prepared Copper oxide nanoparticle. On combined treatment of CONP (0.01 mg/mL) and NIR radiation more of the cells became circular in shape, a clear indication that NIR radiation was successful in generating heat via Copper oxide nanoparticle, inhaled as a model drug compound (Fig. 4.7e). On increasing the CONP concentration to 0.05 mg/mL, a great extent of B16F10 cell lines became affected through toxic nature of Copper oxide nanoparticle which is reflected in their altered morphology from elongated to circular (Fig. 4.7c). On subsequent exposure with 975 nm laser light these nanoparticles induce cellular damage to B16F10 cancer cell lines through photothermal heat generation and most of the cells became destructed (rounded in shape rather than elongated). Figure 4.7f indicates at higher concentration of CONP, through photothermal effect cancer cell death can be achievable through localized heating.

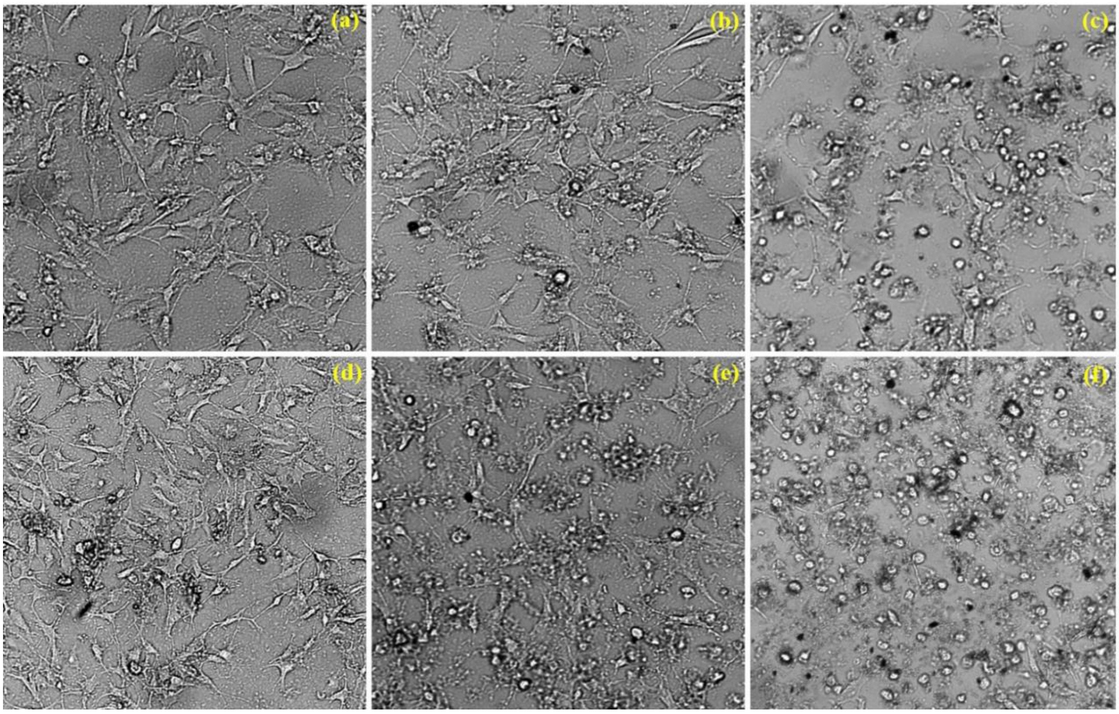

Figure 4.7 Bright field images demonstrating the morphology change process of B16F10 melanoma cancer cells with or without treatment of CONP drug and NIR radiation. **(a)** Bright field image of fully growth cancer cell lines without exposure of CONP drug and NIR laser (negative control) **(d)** Control cell lines with exposure of NIR radiation (positive control) **(b)** cancer cell lines incubated with 0.1 mg/mL concentration of CONP **(e)** Cell lines after combined treatment of 0.01 mg/mL of CONP + NIR radiation **(c)** cancer cells on only exposure to 0.05 mg/mL of CONP **(f)** altered morphology of B16F10 cells by combined treatment of CONP (0.05 mg/mL) + 975 nm laser light.

4.3.5 Viability of B16F10 cancer cells after photothermal treatment

The cell viability assay (MTT assay) was performed on two groups of B16F10 melanoma cells, with and without NIR light exposure (Fig. 4.8). The first group comprised of B16F10 cells was kept in dark (no NIR exposure), and the other group, exposed to NIR light, after incubation with different concentration (0.01-0.05 mg/ mL) of CONP. In addition to these groups, an additional set of control samples was also prepared, those were not exposed to CONP. The cell viability data represented in figure 4.8a, indicates insignificant variation in cellular viability for control samples (both positive and negative). That is both positive as well as negative control sample without exposed to

CONP toxicity are almost unaffected by NIR laser, since cells are transparent to this radiation. But as we traversed from control sample to CONP exposed cell lines (at low concentration region) the cytotoxic effect of drug can be clearly distinguishable. This phenomena is already been represented in bright field image earlier. However combination of CONP+NIR radiation can induced more cell death than CONP alone as established from the cell viability study (depending upon significant cell death level between two cell groups under dark and under irradiation). Interestingly at higher concentration of CONP (≥ 0.04 mg/mL) toxicity of Copper oxide nanoparticle towards cancer cell lines is clearly differentiated as compared to low concentration dosage. The viability is reduced upto ~79 % as compared to control sample due to toxic effect of CONP towards B16F10 cells at higher dosage (≥ 0.04 mg/mL). Upon combined treatment with NIR irradiation this viability is further reduced to ~53 % indicating photogenertaed heat is effective in destruction of cell lines. The two way ANOVA analyses also suggests significant ($P < 0.0001$) drop in viability of B16F10 cells upon laser treatment, incubated with higher dosage of CONP. On further increasing the concentration of CONP more than 50 % cell death activity could be achieved through photothermal effect as shown in figure 4.8a. Earlier bright field images acquired at high concentration level of CONP (Fig. 4.7c & f) indicates the best efficacy of photothermal therapy for treatment of B16F10 cancer cells.

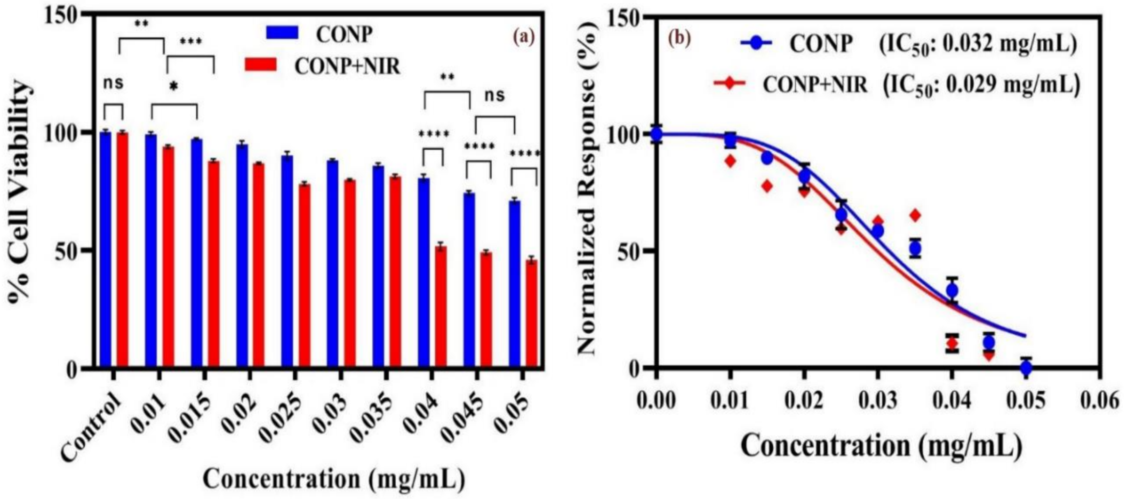

Figure 4.8 (a) MTT analysis of B16F10 cancer cells upon exposure to different concentration of CONP and (CONP + NIR) dosage. Two-way ANOVA was performed by Tukey's multiple comparison test for statistical differences (*p < 0.05, ***p < 0.005, ****p < 0.0001, ns-non significant). **(b)** IC_{50} analysis of B16F10 cells on exposure to different concentration of CONP under dark and NIR irradiated condition.

Furthermore, the half maximum inhibition concentration (IC_{50} analysis) of B16F10 cells, incubated with different dosage of CONP, under dark and NIR light exposure was evaluated using published protocol [268, 286]. The IC_{50} results (Fig. 4.8b) for the cell-lines incubated with CONP under dark are found to be ~0.032 mg/mL. On the other hand same population on exposure to NIR light showed IC_{50} value of ~0.029 mg/mL (Fig. 4.8b). It is explicitly visible that there is close resemblance between optimum concentration calculated from MTT and IC_{50} analysis. Therefore when B16F10 cell-lines are incubated with ≥ 0.04 mg/mL of CONP, significant photothermal efficacy can be achieved without much effort from CONP toxicity. Nevertheless apart from one or two reported researches [219, 220] there is no work till now regarding use of plasmonic Copper oxide nanoparticle as photothermal agent for tumor ablation purpose. Moreover these reported researches are based on additional use of photothermal agent (PDA) and high energetic lasers to archive desired objective. Hence this study is first of its kind where use of less expensive 975 nm CW-diode laser induce heat generation effect.

Additionally, use of NIR radiation would allow deep tissue penetrability thus making study reliable in case of real samples.

Further use of the interesting photo-physical property of CONP harnessed in terms of its electrochemical storage potential.

4.3.6 Electrochemical performance of Copper oxide nanoparticle

Synthesized CONP was evaluated for its redox activity by cyclic voltammetry (CV) using electrochemical workstation. The potential window between -0.8 V to 1V and voltage scan rate of 5 mV/s to 50 mV/s was chosen considering material stability. The response obtained from the CV experiments are shown in figure 4.9. The CONP undergoes series of oxidation and reduction reactions as shown by several anodic and cathodic peaks respectively (figure 4.9a). The redox behaviour displayed by CONP very well resembles with the battery type material, with the distorted rectangle reprsenting the slight EDLC (electrostatic double layer capacitance) type nature. Morevover with in increase in voltage scan rate, the redox peak observed to be increased demonstrating improved rate performance and reversibility involved in fardic redox reaction occuring in the electrode material [324]. With increase in scan rate, the anodic and cathodic peaks are also slightly shifted to right and left region respectively indicating quasi-reversible nature of redox reaction occuring and electrode polarization process [325]. Usually the shift in anodic and cathodic peaks is observed due tokinetic limiation of diffusing electrolyte ions to interact with electrode material. On the contrary at slow scan rates, both electrode and electrolyte ions get enough time to interact [298]. Based on the CV data and previously reported results, the redox peaks are mainly originated due to transition between different oxidation states of Cu atom present in the Copper oxide nanoparticle. The redox peak situated close to 0.01 and 0.4 V (Fig. 4.9a) corresponds to oxidation of Cu (0) → Cu (I) and Cu (I) → Cu (II) species, respectively. While the cathodic peak observed near – 0.1 and 0.2 V indicates the reduction of Cu (II) → Cu (I) and Cu (I) → Cu (0) state respectively. This set of redox reactions corroborate the presence of some amount of Cu2O [295] phase in the synthesized nanoparticle. More precisely set of anodic peaks at -0.3 and -0.03 V indicate the oxidation of copper atom Cu (0) → Cu (I) and Cu (I) → Cu (II) present in CuO . The corresponding reduction peaks obtained at -0.35 and -0.6 V for Cu (II) → Cu (I) and Cu (I) → Cu (0) species respectivly [326]. Based on these observations, a faradic redox mechanism has been proposed for electrochemical reaction within the potential range -0.8 - 0 V [326, 327]

Anodic reactions

$$Cu + CuOH + 2OH^- - e^- \rightarrow Cu_2O + 2H_2O \qquad (5)$$

$$Cu_2O + CuOH + 3OH^- - 3e^- \rightarrow 3CuO + 2H_2O \qquad (6)$$

Cathodic Reactions

$$3CuO + 2H_2O - 3e^- \rightarrow Cu_2O + CuOH + 3OH^- \qquad (7)$$

$$Cu_2O + CuOH + H_2O - 3e^- \rightarrow 3Cu + 3OH^- \qquad (8)$$

Further, another set of redox peaks within -0.1 – 0.4 V range, has led to the development of additional electrochemical reaction mechanisms [299, 325]. Moreover redox peak beyond 0.6 V indicates the formation of Cu (III) soluble species [328].

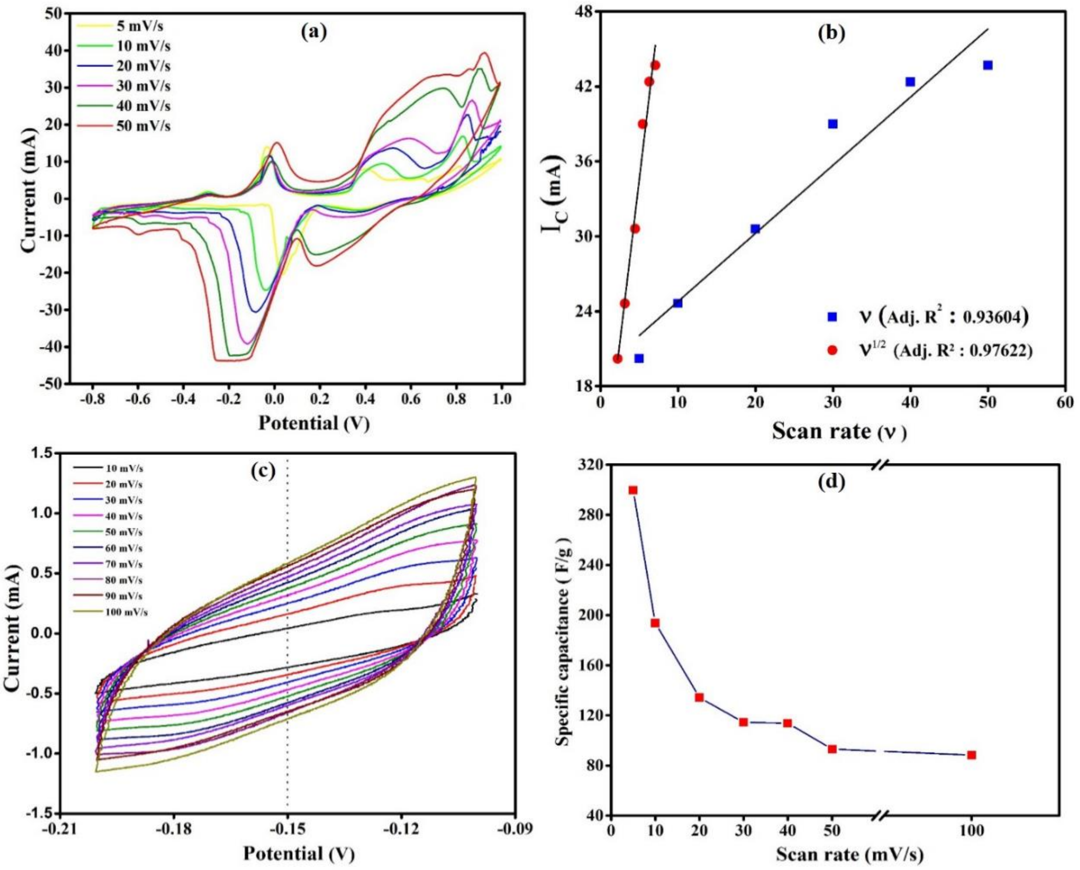

Figure 4.9 (a) CV analysis of CONP electrode in 1M KOH electrolyte at diiferent scan rates. (b) Variation cathodic current with scan rate (c) Cyclic voltammetry analysis performed at open circuit potential for ECSA estimation. (d) Rate performance of CONP electrode.

Similarly, squarewave voltametry plot (Appendix B2) indicates reduction peak near -0.2 V resembling majority of cupric oxide phase in the electrode material [329]. Linear relation between cathodic peak current (I_{CP}) Vs. scan rate (ν) / $(\nu)^{0.5}$ (Fig. 4.9b) indicates that elctrochemical reaction occuring on the Copper oxide electrode are being controlled by surface redox reactions and ion diffusion process [330-332].

While exploring CONP electrochemical performance for possible usage in energy storage devices, quantification of the electrochemical active surface area (ECSA) is very much important [333, 334]. As previously reported a non-faradic charging process was adopted for ECSA estimation, by running different CVs at different scan rates within open circuit potential range particular for Copper oxide [335, 336]. The electrochemical active surface area is calculated to be 0.13 cm^2 (Fig. 4.9c & *Appendix* B3). This value is found to be high enough, for effectively carrying out electrochemical reactions as compared to surface area of other Copper oxide nanoparticles reported earlier [337, 338].

The specific capacitance value of the developed electrochemical cell is obtained from the CV curves at different voltage scan rates and calculated according to equation 9.

$$C_s = \frac{A}{2mk\,(V_2 - V_1)} \qquad (9)$$

where C_s = Specific capacitance (F/g)

A = area enclosed within CV curve ($\int I.dV$)

m = mass of active material loaded onto the working electrode (mg)

k = voltage scan rate (mV/s)

V_2-V_1 = total voltage range or potential window for CV analysis.

As the scan rates increases the redox peaks progressively increases too, due to improved electron transfer rate and good reversibility of faradic reaction process [324, 339]. It is important to note that at high scan rate there is an increase in peak current density, indicating both capacitive and faradic nature of voltammetry current [340]. However with increase in voltage scan rate the specific capacitance value tend to decrease (Fig. 4.9d), which indicates CONP's better rate capability [341]. The underneath mechanism is postulated to be higher residence time of electrolyte ion to interact with active material of electrode in low scan rate unlike high scan rate and limited diffusion of electrolyte ion at high scan rate [300, 342].

Figure. 4.10a represents galvanostatic charge-discharge (GCD) behavior of CONP electrode, measured at various current densities. Entire GCD curves are generated at two different sets of applied current in micro as well milliampere range. The nature of the demonstrated GCD curve is nonlinear unlike perfect triangular shape in case of electrostatic double layer capacitance (EDLC) type material. Hence demonstrating battery type behavior of prepared nanoparticle [324], when used as electrode material where redox reaction is accomplished through faradic mechanism. The initial drop in discharge curve may be correlated with different constraints such as internal resistance offered by CONP, internal connection resistance, resistance due to ion diffusion, and bulk solution resistance as well [330, 343]. As we traverse from low current density to high current density region, the discharging time for stored electrochemical charge is reduced due to obvious reasons. The specific capacitance values at different current densities are calculated from the GCD curve using equation 10.

$$C_s = \frac{\mathbf{I \times t_d}}{\mathbf{m \times \Delta V}} \qquad (10)$$

where C_s = specific capacitance (F/g)

t_d = discharge time

m = mass of active material loaded onto the working electrode

ΔV = stability potential window

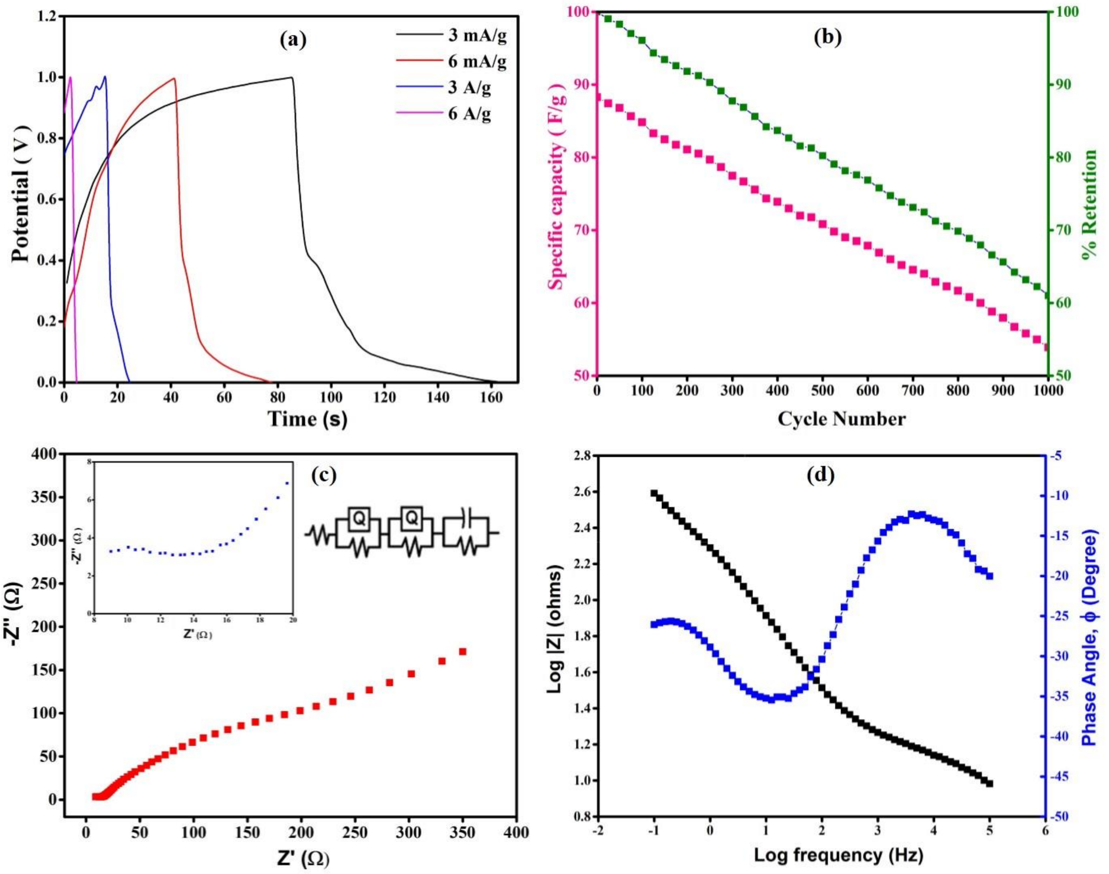

Figure 4.10 (a) GCD curve of CONP electrode in 1M KOH electrolyte. (b) Specific capacity retention over different cycles of operation (c) Nyquist plot and equivalent circuit diagram (inset) (d) Bode plot corresponding to CONP electrode.

The value of specific capacitance for CONP electrochemical material are comparable to that of value obtained from CV curve (Table 4.1).Notice, that with the increase in current density, specific capacitance value decreases, for both micro, as well miliampere current range . However the effect is quite prominent in miliampere current range. As earlier mentioned the charge storage mechanism in Copper oxide nanoparticle based electrode is in accordance to faradic redox mechanism. At small current density, low concentration polarization leads to increase in charging time. Hence due to abundance availability of ions in the vicinity of electrode-electrolyte interface redox transitions of Copper oxide nanoparticle enhanced and thus there is increase in capacitance value. Alternately, it can be proposed that with the reduction of discharging time (t_d) [at high current density] lead to smaller specific capacitance value, since both, discharge time and current density have proportional correlation as mentioned in equation 6 . Same has been observed earlier during cyclic voltammetry analysis.

Two essential factors useful for judging the effectiveness of the electrochemical process of battery/pseudocapacitor are specific energy (E_s) and power density/specific power (P_s). As these parameters are directly related with the charge storage and delivery capacity of the device [344], hence calculated as per equation 11 & 12.

$$E_s = \frac{1}{2} CV^2 \qquad (11)$$

$$P_s = \frac{E_s}{t_d} \qquad (12)$$

Where E_s = Specific energy (Wh/kg)

P_s = Specific power (W/kg)

C = specific capacitance (F/g), V = stable potential rnage (V)

t_d = discharge time (s)

Table 4.1 Comparative study of diiferent electrochemical device paramteres derived from GCD curve of CONP electrode.

ν (mV/s)	C_s (F/g) (CV curve)	Current density (A/g)	C_s (F/g) (GCD Curve) (100 mA)	E_s (Wh/kg)	P_s (W/kg)	η_c (%)
5	247.2549	0.003	0.227	0.038	1.779	90.07
10	171.14379	0.006	0.220	0.037	3.558	89.59
20	126.16013	3	31.41	21.115	7117.44	56.84
30	108.15904	6	18.29	12.297	14,235.19	50
40	101.20915					
50	69.94771					
100	40.14052					

From the table 4.1 it is observed that with increase in current density, the specific energy value decreases and specific power value increases. For a low range of current (microampere scale), change in these values are nominal. Generally, supercapacitors have high power density and batteries exhibit high energy density value. To complement each other’s shortcomings and for the fabrication of portable energy storage device the concept of hybrid-supercapacitor arises. Hybrid supercapacitor generates high power density or specific power value without compromising its energy density output [324, 345] In the present case CONP has simultaneously exhibited excellent specific energy (~20 Wh/kg) and specific power (> 10000 W/kg) values comparable/higher than other reported research [300, 325, 342]for its practical usability as a hybrid supercapacitor. The columbic efficiency (η) (Table 4.1) estimated from the charging discharging time indicates the decrease in efficiency with increase in current density. This might have resulted due to higher concentration polarization, and the irreversibility in charging-discharging process. Columbic efficiency (η) can be calculated using equation 13.

$$\eta\ (\%) = \frac{t_d}{t_c} \times 100 \qquad (13)$$

where t_d and t_c are discharging and charging time respectively.

The cyclic stability of CONP electrode was examined by carrying out CV measurements for about 1000 cycles at a scan rate of 100 mV/s (Fig. 4.10b). The specific capacitance as well retention capacity value for this repeated cycles indicate the CONP stability as an electrode material. From figure 4.10b it is witnessed that with the increase in number of cycles of current-voltage, the measured the specific capacitance value gradually decreases, most likely due to degradation of electrode material, after repeated experiments Additionally we can say that after repeated oxidation reduction measurements, there is a possibility of change in volume of active material deposited on the electrode. Thus it has led to inefficient binding with the Nafion matrix, ultimately decreasing capacitance value [325]. However the retention of specific capacitance value is found to be more than 60 %, even after 1000 cycles of operation.

Furthermore, electrochemical impedance spectroscopy (EIS) was carried out to investigate the electrochemical performance of CONP electrode, its conductivity and ion transfer kinetics at electrode-electrolyte interface [299, 342]. The EIS plot (Fig. 4.10c) exhibits a quasi-semicircle curve at high frequency region and point of intersection of semicircle with the real impedance (Z) axis resulted equivalent series resistance (R_{ES}). The charge transfer resistance (R_{CT}) value is often represented by the diameter of the semicircle. The semicircle in the Nyquist plot refers to the primary resistance offered by electrode material during electrochemical operation. The magnitude of ESR controls the total power performance and energy efficiency. Presence of semicircle indicates the “interfacial contact resistance” between current collector and active material as well as charge transfer resistance. An inclined line following the semicircle is obtained near low frequency region known as “Warburg impedance” (W_R) arising due to diffusion resistance. High value of R_{ES} (~ 7 Ω) could be the reflection of intrinsic resistance offered by electrolyte as well active material and ineffective contact between active electrode material with current collector [342]. Whereas low value of R_{CT} (~ 4 Ω) indicates better ionic conduction and feasible diffusion of electrolyte ions through electrode. The less than 45° angle of “Warburg” line corroborates with the fact that electrode is not solely controlled by ion diffusion as earlier mentioned.

Table 4.2 Values corresponding to series of resistive, capacitive and constant phase elements.

R (Ω)	Q (F)	R (Ω)	Q (F)	R (Ω)	C (F)	R (Ω)
2.484	3.095E-6	12.02	0.001	322.5	0.009	252

The point at which the extrapolated quasi semicircle cuts the real Z (impedance) axis is the equivalent series resistance (RS). Charge transfer resistance (Rct) is obtained from the diameter of the semicircle. Nyquist plot was fitted with the help of “Zsimpwin” software to derive the electrical equivalent circuit diagram. Fitted Nyquist plot arranged in terms of equivalent circuit diagram consists of series of resistive (R), capacitive (C) and constant phase elements (Q) with the values provided in table 4.2.

The variation of impedance and corresponding phase angle with applied frequency is represented in terms of complex plane plot/bode plot (Fig. 4.10d). The slope of log (Z) Vs. log (f) is less than 1, hence exhibiting pseudocapacitive nature of electrode material [297]. Additionally there is huge deviation from the ideal capacitive behavior where phase angle Φ found to 90° [346].

4.4 Conclusion

In conclusion we have demonstrated synthesis of ~13 nm large CONP using *M.oleifera leaf extract* and analytically shown that, prepared CONP contain 80% CuO and 20% Cu_2O phases. The plasmonic character, defect states and indirect band structure of CONP efficiently converted the 975 nm light to heat energy with ~22.6 % conversion efficiency. Herein we have clearly shown that the synergistic effect of small amounts of CONP (0.03 mg/mL) and heat generated, is the cause for 50% damage of B16F10 melanoma cells studied. Besides in this work we have also demonstrated that superior photophysical property imparted hybrid supercapacitor nature to the CONP electrode in an electrochemical workstation. Further CONP electrode resulted in an impressive cyclic stability over 1000 cycles of operation and enhanced power as well as energy density output. Lastly, through this work we have successfully demonstrated that problems in multiple areas can be efficiently & economically tackled by choosing proper material and efficient process engineering approach.